L-shell photoionization of Mg-like S^{4+} in ground and metastable states: Experiment and theory

J.-P. Mosnier[*] and E. T. Kennedy[†]
School of Physical Sciences, National Centre for Plasma Science and Technology (NCPST), Dublin City University, Glasnevin, Dublin 9, Ireland

D. Cubaynes[‡] and J.-M. Bizau[§]
Institut des Sciences Moléculaires d'Orsay, UMR 8214, Rue André Rivière, Bâtiment 520, Université Paris-Saclay, 91405 Orsay, France and Synchrotron SOLEIL, L'Orme des Merisiers, Saint-Aubin, Boîte Postale 48, CEDEX, F-91192 Gif-sur-Yvette, France

S. Guilbaud[‖]
Institut des Sciences Moléculaires d'Orsay, UMR 8214, Rue André Rivière, Bâtiment 520, Université Paris-Saclay, 91405 Orsay, France

M. F. Hasoğlu[¶]
Department of Computer Engineering, Hasan Kalyoncu University, Gaziantep 27010, Turkey

C. Blancard[**]
CEA, DAM, DIF, F-91297 Arpajon, France and Université Paris-Saclay, CEA, LMCE, F-91680 Bruyères-le-Châtel, France

T. W. Gorczyca[††]
Department of Physics, Western Michigan University, Kalamazoo, Michigan 49008, USA

(Received 14 June 2022; accepted 2 September 2022; published 23 September 2022)

We report measurements of the absolute photoionization cross sections of magnesiumlike S^{4+} over the 158–280 eV photon energy range. The experiments were performed with the multianalysis ion apparatus at the SOLEIL synchrotron radiation facility. Single- and double-ionization ion yields produced by the photoionization of the $2p$ subshell of the S^{4+} both from the $2p^6 3s^2\ ^1S_0$ ground state and the $2p^5 3s 3p\ ^3P_{0,1,2}$ metastable levels were observed, as well as $2s$ excitations. Theoretical calculations of the photoionization cross sections were carried out using multiconfiguration Dirac-Fock and *R*-matrix computer codes and the results are compared with the experimental data. While in general reasonably good agreement was found, notable differences in the strengths and positions of predicted resonances were observed and significant systematic energy shifts of the theoretical predictions were required.

DOI: 10.1103/PhysRevA.106.033113

I. INTRODUCTION

Most of the matter in the universe is in the ionized state. Where ions exist near short wavelength sources, the interaction of the ionizing radiation with free positively charged ions becomes of particular importance. The XMM-Newton and Chandra x-ray observatories continue to provide spectrally resolved information on ions within environments such as diffuse interstellar and intergalactic media, active galactic nuclei, planetary nebulae, or areas of star formation [1,2]. The XRISM and Athena future missions will provide greater sensitivity and higher spectral resolution and place even greater demands on relevant atomic theoretical and experimental laboratory investigations, in order to realize their full potential for insights into fundamental cosmic phenomena [3]. The plasma modeling of radiation dominated regions similarly depends on the detailed knowledge of various photon-ion interactions [4]. The overall growing multiple atomic and molecular data needs have led to significant developments, both theoretical and experimental, in laboratory astrophysics [5–7] and atomic databases [8,9] including the investigation of the photoionization behavior of a wide range of important ions [10,11].

Different theoretical models may be used when calculating photoionization of atomic ions, and the value of absolute cross-section measurements, apart from providing basic atomic data for the interpretation of photon-ion interactions in plasma environments, is that they provide benchmarking for the theoretical models. This is important because many of the

[*]Corresponding author: jean-paul.mosnier@dcu.ie
[†]eugene.kennedy@dcu.ie
[‡]denis.cubaynes@universite-paris-saclay.fr
[§]bizau.jean-marc@orange.fr
[‖]segolene.guilbaud@universite-paris-saclay.fr
[¶]mfatih.hasoglu@hku.edu.tr
[**]christophe.blancard@cea.fr
[††]thomas.gorczyca@wmich.edu

cross sections used for astrophysical modeling are generated through computational methods [8,9,12–14]. Inner-shell and double excitations can result in several open atomic shells and this, combined with electron correlation and relativistic effects, places considerable demands on theory. Photoionization cross sections also provide data on the inverse process of dielectronic recombination which can be very important in plasma equilibrium modeling [15,16].

Experimentally, the dual laser plasma (DLP) technique provided early insight into the photoabsorption behavior of a range of positively charged ions [17]. The ongoing need for *absolute* photoionization data on ions prompted significant developments at synchrotron facilities. Pioneered at Daresbury during the 1980s, the merged photon-ion beam approach proved very successful and dedicated systems were installed at SuperACO (Orsay, France), Astrid (Aarhus, Denmark), SPring-8 (Hyogo, Japan), the Advanced Light Source ALS (Berkeley, USA), SOLEIL (St Aubin, France), and most recently at Petra III (Hamburg, Germany) ([18,19], and references therein). In this technique, the ionizing synchrotron radiation beam is overlapped with a charge-selected, counterpropagating beam of ions. By measuring the parameters of the overlapped beams and the resulting photoions, it is possible to provide absolute cross-section values for the different (single, double, etc.) photoionization channels.

Sulfur is an important element in the cosmos, featuring in the top ten elements according to abundance. It can appear in atomic or molecular forms or as part of aggregates [20–23]. Photoionization of specific sulfur atomic ions has been the subject of several studies to date. Resonant photoionization of singly ionized sulfur has been investigated theoretically [24] and experimentally [25]. Photoionization of the triply ionized sulfur ion S^{3+} has been investigated theoretically using the Breit-Pauli method [26]. Previous work on S^{4+} includes the theoretical calculation of oscillator strengths and photoionization cross sections along the magnesium sequence (including S^{4+}) [27] and the calculation of the valence absorption spectrum of S^{4+} [28,29]. Doubly excited autoionization resonances for the S^{4+} isoelectronic cases of Al^+ and Si^{2+} [30] and photoionization spectra in the UV range for the Mg-like Al^+ [31] were also investigated theoretically. Experimental investigations of the $2p$-subshell photoabsorption of the isoelectronic Al^+ and Si^{2+} were carried out using the DLP technique [32,33] and for the Al^+ by the synchrotron photon-ion merged-beam technique [34–36]. More recently, isoelectronic doubly ionized Si^{2+} absolute cross sections and resonance structures were measured at relatively high spectral resolution at the SOLEIL synchrotron and compared to multiconfiguration Dirac-Fock (MCDF) and random-phase approximation calculations [37].

It is the synchrotron-based study of the photoionization of magnesium-like quadruply charged ions of sulfur (S^{4+}) that is the subject of this work. We report the measurement of absolute cross sections for S^{4+} in both single- and double-ionization channels, between photon energies of 158 and 280 eV. This photon energy range lies in the vicinity of the $2p$ and $2s$ inner thresholds and leads to a series of strong resonances, which have been classified and interpreted through concomitant MCDF and R-matrix calculations.

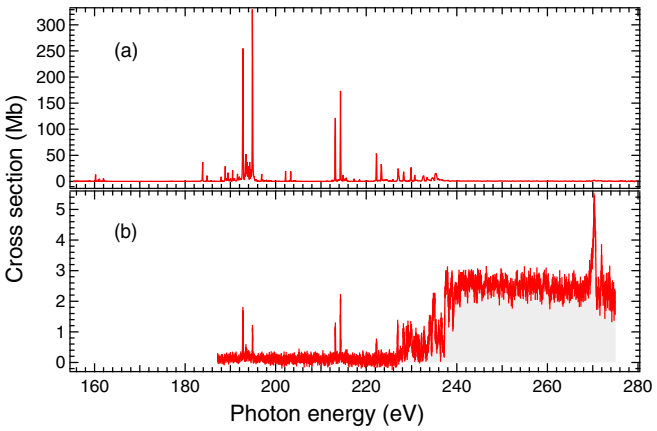

FIG. 1. The measured (a) single and (b) double absolute photoionization cross sections of S^{4+} over the whole photon energy range covered in this work.

II. EXPERIMENTAL DETAILS

A detailed description of the MAIA (Multianalysis ion apparatus) experimental setup and procedures used in our merged-beam measurements can be found in [38]. Briefly, the experimental details relevant to the present study are as follows. The sulfur ions were produced, from hydrogen sulfide gas, in a permanent magnet electron cyclotron resonance (ECR) ion source excited by a 12.36 GHz microwave power supply, run at a power of about 8 W. After extraction and acceleration through a potential difference of −4 kV, quadruply charged S^{4+} ions of terminal velocity 3.1×10^5 ms^{-1} were selected using a magnetic filter and guided by an electrostatic deflector to merge with the counterpropagating synchrotron radiation beam. A typical S^{4+} ion current of 400 nA was achieved. The two beams overlap in a spatially well-defined, 0.57-m long, interaction region. The parent S^{4+} ions were collected in a Faraday cup and the S^{5+} and S^{6+} photoions were counted with a microchannel plate. Photon energy scans of the S^{5+} and S^{6+} count rates map out the single- and double-photoionization cross-section behaviors, respectively. By measuring the photon and ion beam parameters, their overlap volumes, and using calibrated photon and ion detectors it was possible to put the measured cross sections on an absolute basis [38] after noise subtraction. A −2.0 kV bias was applied to the interaction region in order to tag the photoions produced within the interaction region from those produced outside the region. The photon energies were calibrated using a gas cell and known argon reference lines [39] and the resonance energies could be determined to within 40 meV. The relative uncertainty in the measured cross sections is generally within 15% [38].

The measured absolute single- and double-photoionization cross sections are presented in Figs. 1(a) and 1(b), as functions of photon energy over the 158–280 eV range, respectively. The figures also show the statistical error bar at each photon energy data point. All the experimental cross sections presented in this work (Figs. 1 and 4–7) are displayed similarly. At the low-energy end of the single-ionization channel, near 162 eV photon energy, weak resonances are observed which, we will see below, originate from $2p$ excitations of S^{4+}

metastable ^3P levels, whereas, at photon energies above about 180 eV, strong Rydberg series of resonances are recorded which are primarily associated with $2p \rightarrow nd$ excitations in ^1S ground state ions. The strongest resonances between 192 and 194 eV and between 213 and 215 eV can also be seen at the same peak energies in the double-ionization channel, Fig. 1(b), but with much lower cross sections than in the single-ionization channel. The double-ionization channel features a strong enhancement of the cross section above about 225 eV, readily identifiable as the onset of the direct $2p$ ionization process. In the following, we will compare in detail the experimental measurements with the predictions from theoretical calculations using different, R-matrix and MCDF, approaches.

III. THEORETICAL METHODOLOGIES

Two distinct theoretical approaches were used to analyze the experimental results. The MCDF approach treats the S^{4+} N-electron problem directly while the R-matrix calculations treat the problem as single electron scattering off the $(N-1)$-electron S^{5+} target. It is interesting in the present context to intercompare the predictions of both, and with the experimental data.

To study L-shell photoionization of S^{4+}, wave functions were constructed for the initial and final states using linear combinations of coupled configurations, or Slater determinants, made up from atomic orbitals. Since the basis description must be small enough to be computationally feasible, the choice of orbitals and configurations is key, geared towards using the minimal number that will reproduce anticipated photoionization features.

From a single-configuration, nonrelativistic (LS-coupled) perspective, the specific processes to be considered are, first, the inner-shell photoexcitation of the S^{4+} ground state.

$$h\nu + 2s^2 2p^6 3s^2(^1S) \rightarrow 2s^2 2p^5 3s^2 nd(^1P) 2s^2 2p^5 3s^2 ns(^1P) \quad 2s 2p^6 3s^2 np(^1P). \tag{1}$$

The absorption lines in (1) are made up of three dominant Rydberg series that are expected as prominent resonances in the photoionization cross section. The latter absorption gives rise to a single, simple $2snp(^1P)$ resonance series that converges to the higher-energy $2s^{-1}$ L-vacancy state. Of the first two series, the $2p \rightarrow nd$ oscillator strength is expected to be at least nine times stronger than the $2p \rightarrow ns$ strength due to angular momentum coupling, or geometrical factors (see, e.g., [40]).

Each intermediate autoionizing, or resonant, state $2p^5 3s^2 nd$ can decay via two qualitatively different Auger pathways. First, there is *participator* Auger decay

$$2p^5 3s^2 nd \rightarrow 2p^6 3s + e^-,$$

in which the valence electron nd *participates* in the autoionization process, thus giving a decay rate that scales as $1/n^3$. On the other hand, *spectator* Auger decay

$$2p^5 3s^2 nd \rightarrow 2p^6 nd + e^-,$$

proceeds via a stronger, n-independent Auger rate, which broadens the entire Rydberg series of resonances below the L edge. The final theoretical calculations included these resonances as well as the $2s^2 2p^5 3s 3pns$ and $2s^2 2p^5 3s 3pnd$ resonances for photoabsorption from the $2s^2 2p^6 3s 3p(^3P_{0,1,2})$ metastable states.

MCDF calculations were performed using an updated version of the code originally developed by Bruneau [41]. Calculations are based on a full intermediate coupling scheme in a jj basis set. Photoexcitation and photoionization cross sections were computed for the electric dipole transitions only, using the Babushkin gauge which corresponds to the length form of the dipole operator in the nonrelativistic limit [42]. The $2s$ and $2p$ photoexcitation cross sections were calculated for the $^1S_0$ level of the $[\mathrm{Ne}]3s^2$ ground configuration and for the $^3P_{0,1,2}$ metastable levels of the $[\mathrm{Ne}]3s3p$ configuration (where $[\mathrm{Ne}] = 1s^2 2s^2 2p^6$ and denotes an electron configuration only). To describe the initial states, the following configuration set was used: $[\mathrm{Ne}]3l3l'$ where $l, l' = s, p, d$. The $[\mathrm{F}]3s^2 3d$, $[\mathrm{F}]3s3p^2$, $[\mathrm{F}]3s3d^2$, $[\mathrm{F}]3p^2 3d$, $[\mathrm{F}]3s^2 nl$, $[\mathrm{F}^*]3s^2 3p$, $[\mathrm{F}^*]3s3p3d$, $[\mathrm{F}^*]3p^3$, $[\mathrm{F}^*]3p3d^2$, and $[\mathrm{F}^*]3s^2 nl'$ configurations were considered to describe the final states photoexcited from the ground state $[\mathrm{Ne}]3s^2\ ^1S_0$, while the $[\mathrm{F}]3s^2 3p$, $[\mathrm{F}]3s3p3d$, $[\mathrm{F}]3s3pnl$, $[\mathrm{F}^*]3s3p^2$, and $[\mathrm{F}*]3s3pnl'$ configurations were retained to describe the final states photoexcited from the $[\mathrm{Ne}]3s3p\ ^3P_{0,1,2}$ levels (where $[\mathrm{F}] = 1s^2 2s^2 2p^5$, $[\mathrm{F}^*] = 1s^2 2s 2p^6$, $n = 4, \ldots, 7$; $l = s, d$ and, $l' = p$). From this set of 41 configurations involving 1531 levels, the one-electron wave functions were optimized using the Slater's transition state method [43]. To evaluate the lifetime of the $[\mathrm{F}]3s^2 3d\ ^1P_1$ and $^3P_1$ photoexcited states, Auger rates were computed using the one-electron wave functions mentioned above. The largest Auger widths of 74 and 50 meV were obtained for the $[\mathrm{F}]3s^2 3d\ ^1P_1$ and $^3P_1 \rightarrow [\mathrm{Ne}]3s$ decay channels, respectively. The direct $2p$ and $3s$ photoionization cross sections were calculated for all the $[\mathrm{Ne}]3s^2\ ^1S_0$ and $[\mathrm{Ne}]3s3p\ ^3P_{0,1,2}$ initial states. For the latter only, the $3p$ photoionization cross section was also taken into account.

For the R-matrix calculations, the same general method was used as in earlier analyses of experimental synchrotron measurements for various inner-shell photoabsorption cases (see, e.g., [44], and references therein). Within the R-matrix protocol, an atomic orbital basis was used consisting of physical orbitals and additional pseudo-orbitals to account for relaxation effects following $2s$ and $2p$ vacancies, keeping in mind the formulation as an $e^- + S^{5+}$ scattering or quasibound (resonance) calculation. For photoionization of S^{4+}, these orbitals are the $1s$, $2s$, $2p$, and $3s$ physical orbitals obtained from a single-configuration Hartree-Fock calculation on the $S^{5+}(1s^2 2s^2 2p^6 3s)$ ground state. Additional *physical* orbitals $3p$ and $3d$ were generated from frozen-core calculations on the $S^{5+}(1s^2 2s^2 2p^6 3p)$ and $S^{5+}(1s^2 2s^2 2p^6 3d)$ excited states. To expand the basis flexibility and to account for inner-shell relaxation, additional $\overline{4s}$, $\overline{4p}$, and $\overline{4d}$ *pseudo-orbitals* were generated from a multiconfiguration Hartree-Fock calculation on the inner-shell-vacancy $2p^5 3s3p$ ionized state of S^{5+}, allowing all single and double promotions from this configuration to other physical orbitals and pseudo-orbitals (e.g., $2p \rightarrow 3p$ and $2p \rightarrow \overline{4p}$) to account for $2p$ orbital relaxation due to the decreased $1s$-electron screening and increased effective charge Z_{eff}.

TABLE I. Computed *R*-matrix energies, recommended NIST energies, and $2p^{-1}$ thresholds inferred from the present quantum defect analysis of experimental Rydberg series (in parentheses). *R*-mat1 and *R*-mat2 refer to the *R*-matrix energies before and after shifting, respectively.

#	State			Photoelectron energy k^2 or $-\kappa^2$ (Ry)				Photon energy $\hbar\omega$ (eV)	
				R-mat1	Shift	*R*-mat2	NIST	*R*-mat2	NIST
	S^{4+}	$1s^2 2s^2 2p^6 3s^2$	$^1S^e_0$	−5.47666	0.14107	−5.33560	−5.33560	0.00000	0.00000
	S^{4+}	$1s^2 2s^2 2p^6 3s3p$	$^3P^o_0$	−4.72097	0.14195	−4.57903	−4.57903	10.29366	10.29366
	S^{4+}	$1s^2 2s^2 2p^6 3s3p$	$^3P^o_1$	−4.71792	0.14226	−4.57566	−4.57566	10.33948	10.33948
	S^{4+}	$1s^2 2s^2 2p^6 3s3p$	$^3P^o_2$	−4.71103	0.14231	−4.56872	−4.56872	10.43392	10.43392
1	S^{5+}	$1s^2 2s^2 2p^6 3s$	$^2S^e_{1/2}$	0.00000	0.00000	0.00000	0.00000	72.5945	72.5945
2	S^{5+}	$1s^2 2s^2 2p^6 3p$	$^2P^o_{1/2}$	0.97090	−0.00611	0.96479	0.96479	85.7212	85.7212
3		$1s^2 2s^2 2p^6 3p$	$^2P^o_{3/2}$	0.98127	−0.00496	0.97631	0.97631	85.8779	85.8779
4	S^{5+}	$1s^2 2s^2 2p^5 3s^2$	$^2P^o_{1/2}$	12.43132	−0.19900	12.23232		239.02557	(*237.5*)[a]
5		$1s^2 2s^2 2p^5 3s^2$	$^2P^o_{3/2}$	12.51946	−0.19900	12.32046		240.22478	(*238.6*)[a]
6	S^{5+}	$1s^2 2s^2 2p^5 3s3p$	$^4S^e_{3/2}$	12.94643	−0.18920	12.75723	12.72949	246.16739	245.78995
7		$1s^2 2s^2 2p^5 3s3p$	$^4D^e_{1/2}$	13.10688	−0.18920	12.87958	12.89839	247.83206	248.08799
8		$1s^2 2s^2 2p^5 3s3p$	$^4D^e_{3/2}$	13.08651	−0.18920	12.89731	12.87730	248.07329	247.80103
9		$1s^2 2s^2 2p^5 3s3p$	$^4D^e_{5/2}$	13.06878	−0.18920	12.91768	12.85871	248.35044	247.54810
10		$1s^2 2s^2 2p^5 3s3p$	$^4P^e_{1/2}$	13.17137	−0.18920	12.94996	12.96019	248.78963	248.92875
11		$1s^2 2s^2 2p^5 3s3p$	$^4P^e_{3/2}$	13.15495	−0.18920	12.96575	12.94350	249.00447	248.70177
12		$1s^2 2s^2 2p^5 3s3p$	$^4P^e_{5/2}$	13.13916	−0.18920	12.98217	12.93266	249.22787	248.55425
13		$1s^2 2s^2 2p^5 3s3p$	$^2D^e_{3/2}$	13.19784	−0.18920	13.00864		249.58802	
14		$1s^2 2s^2 2p^5 3s3p$	$^2D^e_{5/2}$	13.22689	−0.18920	13.02863		249.86000	
15		$1s^2 2s^2 2p^5 3s3p$	$^2P^e_{1/2}$	13.21783	−0.18920	13.03769		249.98327	
16		$1s^2 2s^2 2p^5 3s3p$	$^2P^e_{3/2}$	13.24280	−0.18920	13.05360		250.19974	
17		$1s^2 2s^2 2p^5 3s3p$	$^2S^e_{1/2}$	13.31425	−0.18920	13.12505		251.17187	
18		$1s^2 2s^2 2p^5 3s3p$	$^2D^e_{3/2}$	13.68799	−0.18920	13.45609		255.67593	
19		$1s^2 2s^2 2p^5 3s3p$	$^2D^e_{5/2}$	13.64529	−0.18920	13.49879		256.25690	
20		$1s^2 2s^2 2p^5 3s3p$	$^2P^e_{1/2}$	13.76438	−0.18920	13.56515		257.15978	
21		$1s^2 2s^2 2p^5 3s3p$	$^2P^e_{3/2}$	13.75435	−0.18920	13.57518		257.29625	
22		$1s^2 2s^2 2p^5 3s3p$	$^2S^e_{1/2}$	13.94185	−0.18920	13.75265		259.71087	
23	S^{5+}	$1s^2 2s2p^6 3s^2$	$^2S^e_{1/2}$	17.40935	−0.58000	16.82935		301.57184	

[a]Experimentally determined value obtained in the present work. See below.

Resultant energies are listed in Table I for the initial S^{4+} ground and metastable states and the S^{5+} scattering target states, as compared to the NIST energies [45]. Since the actual quantity used in the *R*-matrix calculations is the photoelectron kinetic energy, k^2, in rydbergs relative to the ground S^{5+} $1s^2 2s^2 2p^6 3s$ target state (or $-\kappa^2$ for bound states), these are first compared to the NIST values. The photon energy $\hbar\omega$ is then related to the binding energy E_b and the photoelectron energy by $\hbar\omega = E_b + \frac{\hbar^2}{2m}k^2$ for photoionization (or $\hbar\omega = E_b - \frac{\hbar^2}{2m}\kappa^2$ for photoexcitation). However, in view of the relative inaccuracy of the *R*-matrix energies E_b and k^2 compared to the more reliable NIST values, the binding energies E_b and the energies of the inner-shell-vacancy states were shifted by the amounts indicated to better align the computed and NIST photoionization energies.

The complete S^{4+} wave function—either for the initial $2p^6 3s^2$ ground state or $2p^6 3s3p(^3P)$ metastable states, or for the $2p^5 3s^2 nd$ intermediate states embedded in the $e^- + S^{5+}$ final continua—was constructed using a basis coupling all S^{5+} target configurations described above to all physical orbitals and pseudo-orbitals, and an additional orbital basis of 60 *R*-matrix-generated continuum orbitals. A variational approach for the expansion coefficients yields the full initial-state wave functions ψ_i and final-state wave functions ψ_f.

Given the computed *R*-matrix initial and final wave functions, and dipole matrix (D) coupling the two, the photoionization cross section σ as a function of photon energy $E = \hbar\omega$, was determined using the golden rule transition rate divided by initial flux, leading to the expression

$$\sigma = \frac{4\pi^2\alpha}{3}\omega|\langle\psi_i|D|\psi_f\rangle|^2, \tag{2}$$

where α is the fine-structure constant. For photoionization from the metastable states, the procedure was essentially the same except now it is possible to have the lower-energy $2p \rightarrow 3s$ resonance absorption:

$$\hbar\omega + 2p^6 3s3p \rightarrow 2p^5 3s^2 3p.$$

Since this appears below the first $2p \rightarrow 3d$ or $2p \rightarrow 4s$ resonances seen in the ground state photoionization, it was possible to isolate the metastable contributions alone in this lower-energy region (at ≈162 eV in Fig. 1).

Participator Auger decay was accounted for in a straightforward manner by explicitly including the $2p^6 3s$ channel

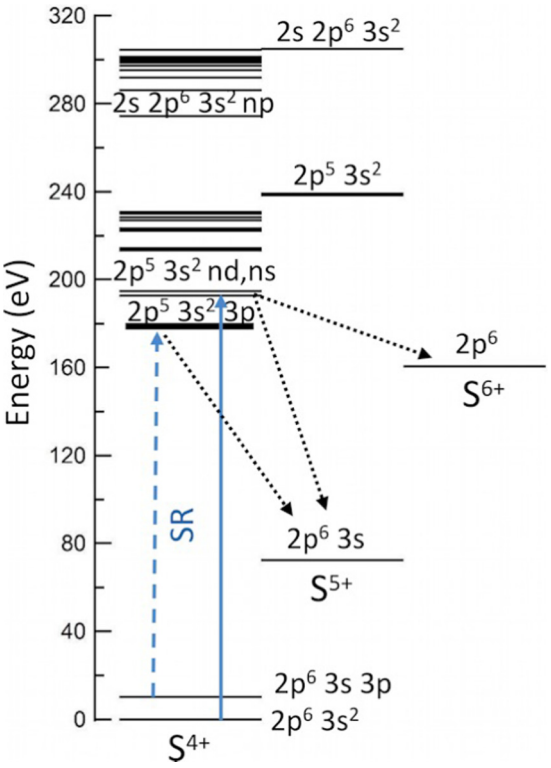

FIG. 2. Schematic energy-level diagram showing excitation energies and ionization thresholds relevant to the present work. The solid and broken blue lines represent possible absorption processes of synchrotron radiation (SR) photons from the S^{4+} $2p^6 3s^2$ ground and $2p^6 3s3p$ metastable states, respectively.

in the standard *R*-matrix implementation [46,47]. Spectator Auger decay was instead included via an optical potential approach [48] that adds an additional imaginary potential $-i\Gamma/2$ to the multichannel quantum defect scattering formulation, with the additional spectator Auger width Γ as an external parameter that can be computed separately or derived from experimental results. Here, it was found that the Lorentzian Auger width is much less than the broader Gaussian width due to experimental broadening, so a fixed spectator Auger width $\Gamma = 2.5 \times 10^{-3}$ Ry $= 34$ meV was chosen that is less than the Gaussian broadening of $\approx$140 meV but larger than the energy mesh step of 1.7 meV used in the final *R*-matrix calculation.

The main excitation, ionization, and decay processes just presented are summarized in Fig. 2 which shows an energy-level diagram for the relevant parent S^{4+}, single-ionization channel S^{5+}, and double-ionization channel S^{6+} ions. The figure shows the metastable $^3P_{0,1,2}$ levels lying just over 10 eV above the $^1S_0$ ground state and indicates the dominant inner-shell excitations $2p^6 3s^2\ ^1S_0 \rightarrow 2p^5 3s^2 nd$, $(n+1)s$ states leading to the $2p^{-1}$ inner-shell ionization limits $2p^5 3s^2\ ^2P_{1/2,3/2}$. Figure 2 also shows the positions of the single- and double-ionization energy values for both valence and inner-shell ionization. For the valence states and ionization limits NIST [45] data are used. The energy bands corresponding with the inner-shell excited states are the results of the present calculations.

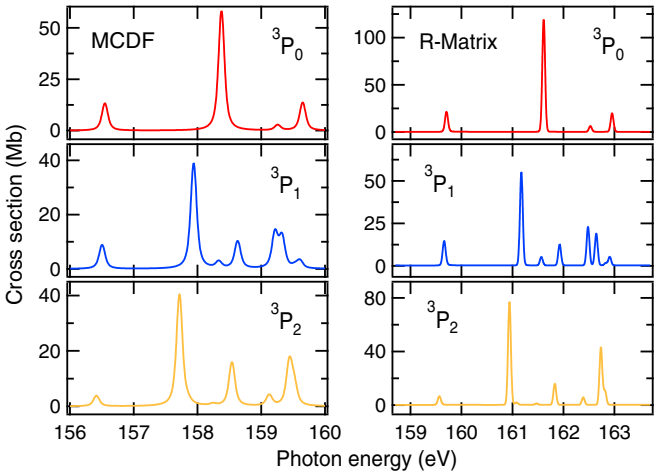

FIG. 3. *Ab initio* MCDF and *R*-matrix cross sections for the $h\nu + 2s^2 2p^6 3s3p\ ^3P \rightarrow 2s^2 2p^5 3s^2 3p\ ^3L^e$ resonances after convolution with a Gaussian function of FWHM 64 meV to simulate the effect of instrumental broadening.

IV. RESULTS AND ANALYSES

In order to examine the experimental data more closely and compare in greater detail with the theoretical predictions of the MCDF and *R*-matrix codes, we divide the overall photon energy scale of Fig. 1 into contiguous photon energy regions, each of which can be associated with a dominant atomic process.

A. Absorption by metastable ions near 162 eV

Metastable ions in sizable amounts can be collisionally produced within the ECR source due to the presence of high-energy electrons therein. The S^{4+} ions in the merged-beam overlap region therefore exist in the ground $(3s^2\ ^1S_0)$ or metastable $(3s3p\ ^3P_{0,1,2})$ states, as the latter can have sufficiently long lifetimes to survive the journey from the ECR source to the overlap region. The presence of excited state parent ions is a well-recognized issue in merged-beam experiments [18,19]. In the present case of S^{4+} ions, there are clearly resolved resonances associated only with photoionization of $^3P_{0,1,2}$ metastable ions observed in the single-ionization channel in the 162-eV photon energy range (see Figs. 1, 3, and 4). Measurements of the strengths of these metastable resonances enable us to estimate the relative populations of ground to excited initial states. We require this information in order to reliably compare the experimental data with the corresponding theoretical predictions (e.g., [49]).

The resonances observed around 162 eV arise purely from the excited $2p^6 3s3p\ ^3P_{0,1,2}$ valence-excited states. We note that the E_1 allowed $3s3p\ ^3P_1 \rightarrow 3s^2\ ^1S_0$ radiative decay has a transition probability of 1.65×10^5 s^{-1} (equivalent to a radiative lifetime of 6.06 μs) [45] which is similar to the transit time from the extractor to the overlap regions of the S^{4+} ions. This decay contributes to repopulating the $3s^2$ ground state along the ions path.

Figure 3 shows the *ab initio* MCDF and *R*-matrix cross sections for the $h\nu + 2s^2 2p^6 3s3p\ ^3P \rightarrow 2s^2 2p^5 3s^2 3p\ ^3L^e$ resonances after convolution with a Gaussian function of FWHM

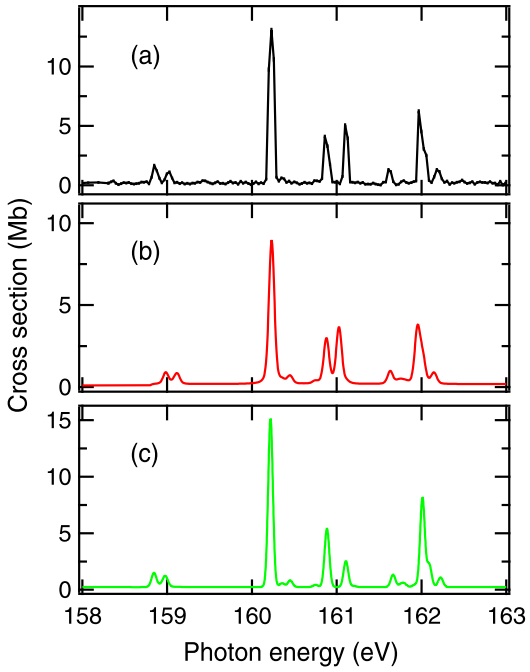

FIG. 4. Photoionization cross sections of S^{4+} in $2p^6 3s3p\ ^3P_{0,1,2}$ initial states: (a) Measured, and (b) and (c) simulated from the results of MCDF and *R*-matrix theoretical calculations, respectively.

(full width at half maximum) 64 meV to simulate the effect of instrumental broadening. A 74-meV Lorentzian profile was used for all the MCDF calculations which is larger than the Gaussian instrumental broadening of 64 meV and accounts for the overall broader MCDF profiles compared with the *R*-matrix ones. Figure 4(a) shows the experimentally observed $2s^2 2p^5 3s^2 3p\ ^3L^e$ resonances. There are marked differences with Fig. 3 in the widths, energy positions, and strengths of the resonances. Overall shifts of +2.5 and −0.7 eV applied to the *ab initio* MCDF and *R*-matrix resonance energies, respectively, bring the main predicted resonances into approximate coincidence with the main experimental resonance at 160.23 eV. The aforementioned difference in resonance strengths is due to the $3s3p\ ^3P_{0,1,2}$ populations relative to the population of ground state ions in the sample beam. By summing the cross sections over the resonances for the experimental profiles and comparing with the analogous integrated cross sections from the MCDF and *R*-matrix predictions, we obtained the estimates for the relative populations of the various levels as 78% $^1S_0$, 4% $^3P_0$, and 18% $^3P_2$. Once these scaling and modeling parameters were determined and applied to the *ab initio* data of Fig. 3, it is seen that the overall structures of the experimental resonances of Fig. 4(a) are quite well reproduced by both the scaled MCDF and the *R*-matrix simulations of Figs. 4(b) and 4(c), respectively. From now on, the same populations scaling parameters are applied to all the theoretical spectra when a comparison with experimental data is made, whereas different energy shifts need to be applied for the different spectral windows under investigation (see details below).

Table II shows a list of all the experimental resonances arising from the metastable states. Energies, line strengths, and widths are provided from the experimental measurements and compared with the MCDF and *R*-matrix calculations. As expected, all the observed features are readily interpreted as originating from either of the two $2p^6 3s3p\ ^3P_{0,2}$ initial states with no discernible contributions from $2p^6 3s3p\ ^3P_1$.

B. Region of $2p \rightarrow 3d$ excitations 184–198 eV

Figures 5(a) and 5(b) show the experimental data acquired with a bandpass of 80 meV, over the photon energy range between 184 and 198 eV, for the single-ionization and double-ionization channels, respectively. The single-ionization channel is shown again in Fig. 5(c) but with a narrower bandpass of 47 meV. Also shown in Figs. 5(d) and 5(e) are the MCDF and *R*-matrix results, respectively, convolved with a 47-meV Gaussian function and appropriately weighted and energy shifted (MCDF +2.5 eV, *R* matrix −1.9 eV). These can be compared with the experimental

TABLE II. Experimental and theoretical energies and line strengths for resonances in the 158–163 eV photon energy range due to $2p \rightarrow 3s$ inner excitations in S^{4+} valence excited in the $2p^6 3s3p\ ^3P_{0,1,2}$ states.

Energy (eV)			Strength (Mb eV)			Initial state
Measured[a]	*R* matrix	MCDF	Measured	*R* matrix	MCDF	MCDF
158.86(5)	159.57	158.18	0.11(2)	0.087	0.046	$^3P_2$
159.02(5)	159.71	158.32	0.07(2)	0.066	0.055	$^3P_0$
160.23(5)	160.94	159.43	1.0(2)	0.955	0.604	$^3P_2$
160.37(7)	161.08	159.56	0.03(3)	0.025	0.013	$^3P_2$
160.75(9)	161.47	159.95		0.013	0.010	$^3P_2$
160.88(5)	161.61	160.08	0.28(5)	0.328	0.248	$^3P_0$
161.11(5)	161.83	160.23	0.33(5)	0.195	0.236	$^3P_2$
161.62(5)	162.39	160.83	0.08(2)	0.069	0.052	$^3P_2$
161.79(9)	162.53	160.97		0.017	0.015	$^3P_0$
161.98(5)	162.73	161.15	0.38(6)	0.527	0.232	$^3P_2$
162.05(5)	162.81	161.21	0.15(3)	0.129	0.128	$^3P_2$
162.19(5)	162.96	161.35	0.09(2)	0.055	0.057	$^3P_0$

[a]The number in parentheses is the uncertainty on the last digit due to the numerical fitting procedure used to determine resonance peak maximum.

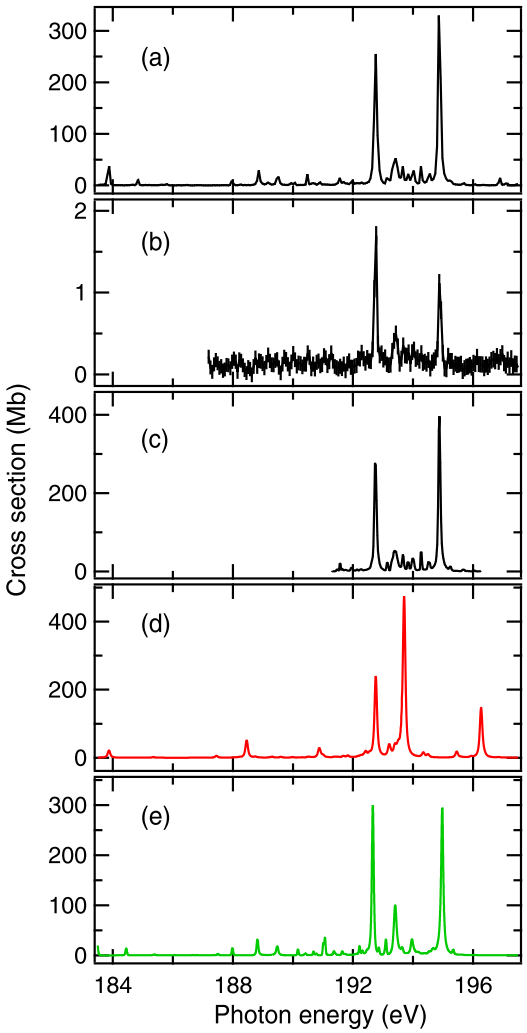

FIG. 5. Photoionization cross sections of S^{4+} in the 188–200 eV photon range (region of $2p \rightarrow 3d$ excitations): (a) and (b) Experimental values measured with 80 meV bandpass for single ionization and double ionization, respectively; (c) experimental values for single ionization measured with 47 meV bandpass; (d) MCDF and (e) *R*-matrix theoretical cross sections, convolved with a 47-meV Gaussian function and weighted according to the initial populations, respectively.

results of Fig. 5(c). From the $3s^2(^1S_0)$ ground state, as expected, the observed resonance structure is comparatively simpler than the more complex structure arising from the $^3P_{0,1,2}$ metastable levels. It is seen that the *R*-matrix simulation agrees well with experiment while the MCDF resonances differ quite significantly.

A list of the most intense ground state resonances observed in this photon energy region is provided in Table III which shows their energies, line strengths, and some assignments. The two main $3s^2 3d\ ^3D_1$ and $^1P_1$ resonances at 192.74 and 194.88 eV, respectively, dominate the experimental spectra. The strength of the spin-forbidden $3s^2 3d\ ^3D_1$ component reflects the importance of spin-orbit mixing effects between terms of different multiplicities of the same configuration. Additional resonances are clearly distinguishable in this range and, following the MCDF theoretical predictions, attributable to strong correlation mixing (configuration interaction) effects between terms of the energetically close $2p^5 3s^2 3d$ and $2p^5 3s 3p^2$ configurations [i.e., the $(3s3d + 3p^2)$ mixing [50]; see Table III].

It is worth pointing out that the extent of mixing between nearby resonances, whether differing in *L* and *S* but still coupling via the stronger spin-orbit operator V_{SO} that scale as Z^4, with $Z = 5$, or coupling the same *L* and *S* via the interelectron operator V_{ee}, is highly sensitive to the relative positions of the mixing states. A simple two-state analysis shows that theoretical predictions for the fractional mixing of any two states is given as $|c_2|^2/|c_1|^2 \approx [V/(E_2 - E_1)]^2$ with $V = V_{ee}$ or V_{SO}, so that two resonances can exchange oscillator strengths, and the relative oscillator strengths are sensitive to the predicted relative energies, which have inherent uncertainties, as has been seen.

C. Region of $2p \rightarrow nd$ Rydberg excitations and $2p$ thresholds 200–244 eV

Figure 6 shows the corresponding data for the 200–244 eV range where the various resonance series are approaching the $2p$ inner-shell ionization limits. The single- and double-ionization channels are shown for the experimental data in Figs. 6(a) and 6(b), respectively. The MCDF and *R*-matrix theoretical results are shown in Figs. 6(c) and 6(d), after appropriate populations weighting and energy shifts (MCDF + 2.5 eV, *R*-matrix −1.9 eV), respectively. Both simulations

TABLE III. Experimental and theoretical energies and line strengths in the188–200 eV photon energy range for the resonances arising from $2p \rightarrow 3d$ excitations in ground state ($^1S_0$) S^{4+}.

Energy (eV)			Width (meV)			Strength (Mb eV)			Final state
Measured	*R* matrix	MCDF	Measured	*R* matrix	MCDF	Measured	*R*matrix	MCDF	*LSJ*
183.87(4)	185.39	180.50		23		3.6(6)	5.51	5.42	$3s3p^2\ ^3P_1$
184.83(4)	186.38	181.38		16		0.8(3)	1.19	3.02	$3s3p^2\ ^3D_1$
187.98(4)	189.91	184.96		8.8		0.7(3)	1.10	0.77	
188.86(4)	190.75	185.97		35		2.7(5)	3.62	7.26	$3s3p^2\ ^1P_1$
189.50(4)	191.41			54		2.2(5)	2.62		
192.74(4)	194.59	190.27	47(1)	43	15.9	31(5)	37.6	33.7	$3s^2 3d\ ^3D_1$
193.42(4)	195.34		149(13)	97		13(2)	22.6		$3s^2 3d\ ^3P_1$
194.88(4)	196.90	191.21	51(1)	84	74.2	46(7)	45	64.9	$3s^2 3d\ ^1P_1$

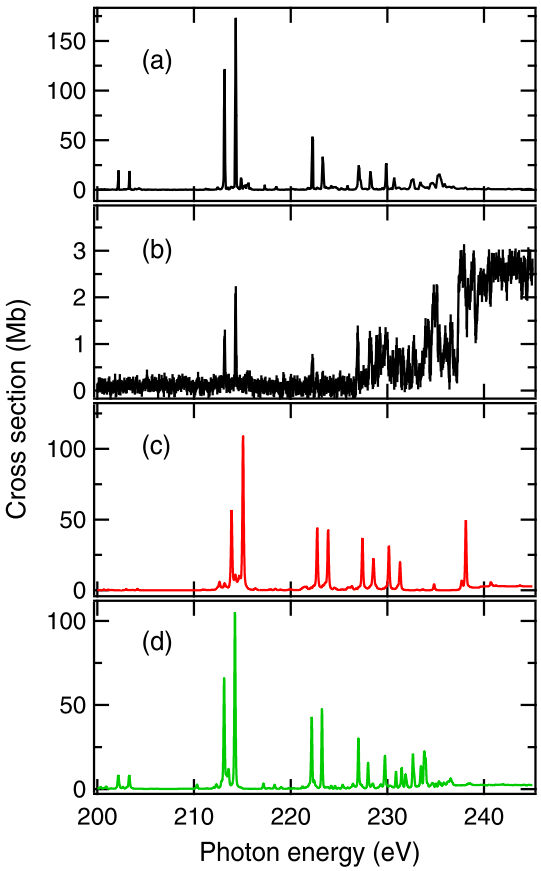

FIG. 6. Photoionization cross sections of S^{4+} in the 200–240 eV photon range (region of $2p \rightarrow nd$ Rydberg excitations and $2p$ thresholds): (a) and (b) Experimental values measured with 110 meV bandpass for single and double ionization, respectively; (c) MCDF and (d) *R*-matrix theoretical cross sections, convolved with a 110-meV Gaussian function and weighted according to the initial populations, respectively.

represent the experimental data quite well with the latter simulation better reproducing the weaker experimental resonances near 203 eV.

Table IV includes a list of the observed resonance energies, relative line strengths, and assignments. The latter are obtained from standard quantum defect (QD) analyses of the experimental and theoretical data and assume, as suggested by visual observations, the existence of four distinct Rydberg series, namely, $2p \rightarrow nd\ {}^1P_1,{}^3D_1$ and $2p \rightarrow (n+1)s\ {}^1P_1,{}^3D_1$ converging on the two $2p^5 3s^2\ {}^2P_{1/2,3/2}$ limits. Quantum defect values of $\mu_d = 0.25$ and $\mu_s = 0.9$ are obtained. The small value of the former indicates more strongly localized hydrogenic orbits for the *nd* Rydberg electron while the larger value of the latter points to more delocalized penetrating orbits for the *ns* Rydberg electrons. The use of the ${}^1P_1$ and ${}^3D_1$ *LSJ* labeling for the designation of these Rydberg series is based on the MCDF eigenvector compositions for the states having the largest $3d$ and $4s\ {}^1P_1$ and ${}^3D_1$ characters, respectively. Although this does not invalidate the present QD analyses, the *jK* or *jj* notations would likely be more appropriate for Rydberg states with $n > 3$ (see [37] for example,; however, such detailed data is not available for S^{4+}).

A comparison of Figs. 6(a) and 6(b), shows that identical intensity patterns at the exact same photon energies are retrieved in the single- and double-ionization channels for the resonant Auger decay of, most evidently, the $4d$ and other *nd* states. This suggests shake-off like processes in the double-ionization channel for these states. Getting closer to the energy of the $2p^5 3s^2\ {}^2P_{1/2,3/2}$ thresholds, supernumerary resonances, i.e., not fitting into the Rydberg patterns just mentioned, are observed. These are discussed in the following section.

In addition to visibly comparing the experimental cross-sectional profile with the theoretical simulations in Fig. 6, which, in principle, requires the theoretical knowledge of the Auger width for each individual resonance, we can quantitatively assess the theoretical atomic data by comparing the integrated cross section over a given photon energy window. This is tantamount to comparing the measured and calculated amounts of oscillator strength in the photon range. The relevant numbers between 190 and 244 eV are as follows: experiment total ionization (sum of single- and double-ionization channels), 149.9 Mb eV; MCDF, 132.8 Mb eV; and *R* matrix, 124.5 Mb eV, i.e., relative differences of 11% and 17%, respectively.

D. Region of the 2*p* thresholds and 2*s* excitations 230–300 eV

Figure 7 shows the details for the 230–300 eV range which overlaps the $2p$ inner-shell ionization limits. The experimental results for single and double photoionization, yielding S^{5+} and S^{6+} ions, are shown in Figs. 7(a) and 7(b), respectively. Above the $2p$ threshold, where single photoionization of a $2p$ electron occurs, the resultant $S^{5+}\ 2s^2 2p^5 3s^2$ ionic core can either (a) decay radiatively via a $3s \rightarrow 2p$ transition, resulting in a S^{5+} final state, or (b) it can autoionize via a $3s^2 \rightarrow 2p + e^-$ Auger transition, resulting in a S^{6+} final state. By using the atomic structure and autoionization code AUTOSTRUCTURE [51] to calculate radiative and Auger rates, the fluorescence branching ratio was computed to be about 0.10, and indeed the two figures above the $2p$ threshold seem to mimic each other in about the ratio of 9:1, which explains the nonzero background cross section seen in the single-ionization cross section. Direct ionization of a $3s$ valence electron may also contribute to the latter; however, with a likely negligible contribution.

As mentioned briefly above, a number of strong resonances with energies just below the $2p$ thresholds are distinctively observed in the single- and double-ionization channels [see Figs. 7(a) and 7(b)]. These resonances are found over the 232–238 eV range and do not fit into the pattern of $2p \rightarrow nd, (n+1)s$ Rydberg series identified above. Several intense and sharp resonances are seen in the single-ionization channel [see Fig. 7(a)] without clear counterparts at the same energies in the double-ionization channel. The double-ionization channel shows the characteristic steplike structure of the onset of continuum Auger processes over the 237–238 eV band of energies. This is compatible with the QD analyses of Table IV which provide experimentally determined ${}^2P_{1/2}$ and ${}^2P_{3/2}$ threshold values at 237.5 and 238.6 eV, respectively. Additional discrete and broad structures are superimposed in the 237–239 eV also [see Fig. 7(b)]. The experimentally

TABLE IV. Experimental and theoretical energies and Rydberg analyses in the 190–240 eV photon energy range for the resonances arising from $2p \rightarrow nd\ ^1P_1,^3D_1$ and $2p \rightarrow (n+1)s\ ^1P_1,^3D_1$ excitations in ground state ($^1S_0$) S^{4+}.

	Resonance energy (eV)					
		$^1P_1$ series			$^3D_1$ series	
Electron excitation	Measured	MCDF	*R* matrix	Measured	MCDF	*R* matrix
$2p \rightarrow 3d$	192.75	190.27	194.59	193.42	191.21	195.34
$4d$	213.17	211.39	215.04	214.31	212.57	216.17
$5d$	222.26	220.24	224.11	223.32	221.37	225.17
$6d$	227.04	224.92	228.93	228.24	226.08	229.94
$7d$	229.92	227.66	232.82	230.7	228.81	233.41
⋮						
∞d	237.3	235.3	239.1	238.4	236.5	240.2
Quantum defect[a]	0.24	0.25	0.24	0.25	0.25	0.25
$2p \rightarrow 4s$	202.27	200.48	204.11	203.41	201.65	205.24
$5s$	217.42	215.26	219.11	218.60	216.45	220.60
$6s$		222.18	226.12		223.38	226.52
$7s$		225.97			227.19	
⋮						
∞s	237.5	235.1	239.1	238.6	236.3	239.6
Quantum defect[a]	0.9	0.86	0.88	0.9	0.86	0.93

[a]Obtained from the numerical fit of the standard hydrogenic energy-level formula.

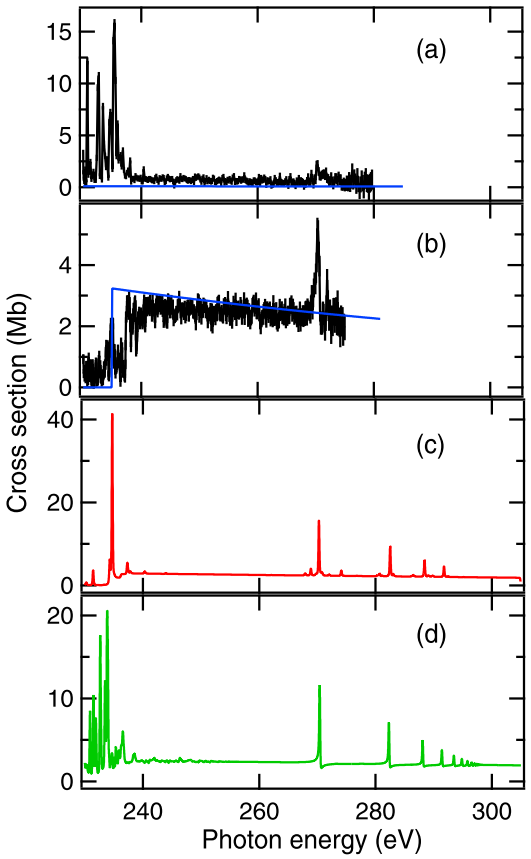

FIG. 7. Photoionization cross sections of S^{4+} in the 235–305 eV photon range (above $2p$ thresholds): (a) and (b) Experimental values measured with 150 meV bandpass for single ionization and double ionization, respectively; the blue traces are the $3s$ and $2p$ photoionization cross sections from Ref. [13]; (c) MCDF and (d) *R*-matrix theoretical cross sections, convolved with a 150-meV Gaussian function and weighted according to the initial populations, respectively.

determined threshold values are reasonably well reproduced by the *R*-matrix and MCDF values of Tables I and IV. We propose that $J = 1$ states obtained from the multiply excited configurations $2p^5 3p^2 nd$, $2p^5 3d^2 nd$, or $2p^5 3s3dnd$ ($n \geqslant 3$) contribute to the patterns of resonances observed in Fig. 7(a). Preliminary MCDF calculations for the $2p^5 3s3d^2$ configuration support this hypothesis, but no detailed theoretical predictions are available at this stage.

We note that the first member of the $2s \rightarrow np\ ^1P_1$ series, namely, the $2s2p^6 3s^2 3p\ ^1P_1$ resonance is predicted at 234.0 and 238.1 eV by the *R*-matrix and MCDF theories, featuring as prominent peaks in Figs. 7(c) and 7(d). The strong resonances lying around 235.0 eV in the single- and double-ionization channels in Fig. 7(a) and 7(b) are thus assigned to the $2s2p^6 3s^2 3p\ ^1P_1$ resonance, accounting for the additional discrete structure observed in the vicinity of the $2p$ thresholds. MCDF predicts the $2s2p^6 3s^2 3p\ ^1P_1$ resonance just above these thresholds while *R* matrix places it just below, which would seem more in line with the experimental observations. Overall, the MCDF and *R*-matrix simulations differ quite markedly in this region [see Figs. 7(c) and 7(d)]; the complexity of the observed structure being generally better simulated by the *R*-matrix results. This is likely related to the overlap of several $2p^5 3s3lnl'\ ^{(2S+1)}L_{J=1}$ Rydberg members with the strong $2s2p^6 3s^2 3p\ ^1P_1$ resonance, which is seen to lie below the $2p^{-1}$ thresholds in the *R*-matrix results, thereby mixing oscillator strengths for a more complicated resonance spectrum. However, a number of important multiply excited configurations would need to be introduced in the calculations to obtain a reliable intercomparison of the theoretical results. Figure 7(b) also includes the prediction of the Verner formula [13], which is seen to match the experimental data well in the continuum region.

In the region from the $2p$ thresholds up to 300 eV, the direct $2p$ ionization process followed by Auger decay dominates as seen by the strength of the continuum

TABLE V. Experimental and theoretical energies in the 235–300 eV photon energy range for the $1s^22s^22p^63s^2\ ^1S_0 \longrightarrow 1s^22s2p^63s^2np\ ^1P_1$ resonances in S^{4+}.

	Resonance energy (eV)		
n	Measured	MCDF	R matrix
3	235.0	238.1	≈234
4	270.3	271.17	272.34
5		283.42	284.24
6		289.33	290.05
7		292.68	293.36
8			295.42
9			296.79
10			297.75
11			298.45
12			298.97
13			299.37
14			299.69
15			299.94
16			300.14
17			300.31
18			300.45
19			300.57
20			300.67
21			300.76
22			300.83
Limit ∞p		301.1[a]	301.6[a]

[a]Quantum defects of 0.63 (MCDF) and 0.59 (R matrix) from numerical fits of the hydrogenic formula.

processes found entirely in the double-ionization channel [see Fig. 7(b) and also Fig. 1(b)]. The discrete pattern of the $2s \rightarrow np\ ^{3,1}P_1$ excitations is superimposed on this continuum. This results in two Rydberg series converging on the $1s^22s2p^63s^2\ ^2S_{1/2}$ inner-shell ionization limit. The latter is predicted to lie just above 301 eV photon energy by both the MCDF and the R-matrix calculations (see Table V). The first member $2s \rightarrow 3p\ ^1P_1$ overlaps the $2p$ thresholds region as discussed above. The $2s \rightarrow 4p\ ^1P_1$ resonance features in both the single- and double-ionization channels as seen in Figs. 7(a) and 7(b), respectively. Higher series members were not intense enough to emerge clearly out of the background noise and are not shown here. The characteristic asymmetric Fano profile shape is observed in Fig. 7(b), pointing to sizable interaction with the underlying continua. However, the experimental profile data appeared to be too noisy to extract reliable Fano parameters for the resonance after deconvolution of the instrumental broadening. Successive resonant Auger decays of the type $1s^22s2p^63s^24p \rightarrow 1s^22s^22p^53s^2 + e^- \rightarrow 1s^22s^22p^6 + e^-$ could be invoked to explain the relative strength of this resonance in the double-ionization channel. The population-weighted and energy-shifted MCDF (−0.9 eV) and R-matrix (−1.9 eV) calculations reproduce the experimental results well as shown in Figs. 7(c) and 7(d), respectively, except for differences discussed below. Resonance energy data is summarized in Table V for the series.

It is worthwhile discussing further the various causes for discrepancies between the experimental and two theoretical results. The main differences are found in the photon energy positions of the resonances. Since computed energy positions of ionic states are determined from variational approaches, there is an inherent overestimation of those energies, and since the photon energy involves the difference between ionic states (e.g., between the $2p^53s^2nd$ ground state and $2p^63s^2$ for the $2p \rightarrow nd$ Rydberg series of resonances), there is a corresponding uncertainty in computed vs converged, or NIST, or experimental, photon energies. Furthermore, since the MCDF and R-matrix calculations rely on separate basis sets of orbitals and configurations, optimized in independent calculations, the predicted energies will differ between the two calculations. Some of these errors are corrected in the R-matrix calculations by using empirical shifts of certain energies to NIST values, but there are still uncertainties associated with the threshold positions of the inner-shell excited S^{5+} states for which no empirical data exist, and also with the computed quantum defects. The photon energy of a resonance of principal quantum number n belonging to the ith excited-state Rydberg series is $\hbar\omega = E_b + [E_i - Z^2/(n - \mu_{n,i})^2]$, where $Z = 5$ is the ionic charge of the S^{5+} residual ion, E_i is the energy of the excited target state (as listed in Table I, for instance), and $\mu_{n,i}$ is the quantum defect of that series member. Despite shifting E_b to align with NIST, and doing the same for some of the E_i as well, other E_i values are unknown (they are autoionizing states), and the quantum defects have their own uncertainties, so resonance position discrepancies are commonplace in general, and only for the smaller, easily converged systems can those uncertainties be brought to within experimental resolution.

As for differences between MCDF and R-matrix results, the MCDF calculation can sometimes include extra configurations, such as $2s2p^63s3pnl$, that would require additional $2s2p^63s3p$ target states in the R-matrix method, resulting in a computationally unfeasible calculation. As a result, those additional $2s2p^63s3pnl$ resonances can be seen faintly in the MCDF results in Fig. 7 but are completely absent in the R-matrix results, where only the $2s2p^63s^2np$ resonances are seen. On the other hand, the R-matrix method implicitly consists of a larger basis than the MCDF approach in one sense. Whereas the MCDF basis set for, say, the $2p^53s^23d$ "resonance" consists of the $2p^53s^2nd$ (n = 3–7) configurations, as well as other two particle–two hole promotions such as the $2p^53s3p^2$ configuration, the R-matrix basis consists of essentially all $2p^53s^2nd$ (n = 3–∞) *and* $2p^53s^2\epsilon d$ configurations, i.e., an R-matrix optimized outer-d orbital. In a similar sense, the MCDF $2s2p^63s^2np$ resonance series shows symmetric Lorentzian profiles in Fig. 7 whereas the R-matrix results include configuration interaction, or interference, between the $2s^22p^63s^2 \rightarrow 2s2p^63s^2np \rightarrow 2s^22p^6np + e-$ indirect resonance pathway and the direct $2s^22p^63s^2 \rightarrow 2s^22p^6np + e-$ photoionization pathway, giving rise to asymmetric Fano resonance profiles, as also seen in the experimental $2s2p^63s^23p$ resonance at 272.34 eV. As a last noticeable difference, the $2s2p^63s^23p$ resonance acts as a perturber, or interloper, with the series limit of the $2s^22p^53s^2nd$ resonance series, and the R-matrix results show a much more pronounced sharing of oscillator strength between the two, which is attributable to the omission of the $2s^22p^63s^2nd$ (n = 8–∞) configurations

in the MCDF calculation. In summary, and especially for challenging 14-electron systems such as S^{4+}, any finite-basis theoretical approach has inherent uncertainties in resonance energy positions and oscillator strengths, and perhaps also in the extent to which configuration interaction is included, leading unsurprisingly to corresponding differences in overall resonance profiles.

V. CONCLUSIONS

Most of the cross sections for atomic ions, needed to model the behavior of many astrophysical and laboratory plasmas, are generated through computational methods. Experimental benchmarking of such theoretical approaches is therefore critical. This is particularly true in the realm of astrophysics, due to the advent of new more powerful satellite x-ray observatories requiring, for their optimum exploitation, reliable fundamental data on the interaction of photons with positively charged ions.

The case of S^{4+} constitutes a particularly nice test bed for a detailed comparison of experimental data with the predictions of different theoretical methodologies. The closed-shell nature of the ground state means that the dominant challenge for theory is to treat the excited states which include both inner-shell and multiple electron excitations.

Using the MAIA merged photon-ion beam facility at SOLEIL we have measured the absolute cross sections for photoionization of magnesiumlike S^{4+} in the photon energy region corresponding to excitation and ionization of the inner-shell $2s$ and $2p$ electrons, in both the single- and double-ionization exit channels. Resonances arising from both ground $^1S_0$ and metastable $^3P_{0,1,2}$ states were observed and the relative populations determined. The results are compared with predictions from two disparate theoretical approaches: the MCDF and R-matrix methods. The former addresses the S^{4+} system directly while the latter treats the problem as electron scattering from a S^{5+} target. Detailed calculations were carried out and the predictions compared with the experimental results, following convolution with the experimental bandpass and weighting to take account of the different initial-state populations. Figures and tables are provided which detail the measured resonance energies and strengths and compare with the theoretical predictions.

The main new findings of this work are as follows and should be understood in the context of the effects of the increasing ionicity of S^{4+} (effective nuclear charge $Z_{\rm eff} = 5$) along the magnesium isoelectronic sequence. The bulk of the discrete oscillator strength was found to lie in the $2p \rightarrow nd$ resonances, $l \rightarrow (l+1)$ excitations, to the detriment of the $2p \rightarrow (n+1)s$ resonances, $l \rightarrow (l-1)$ excitations which were very weak. Most of the $2p \rightarrow nd$ resonances were seen to fit reasonably well regular Rydberg series converging on the $2p^{-1}\,{}^2P_{1/2,3/2}$ limits. Strong departures from this behavior were observed in (1) the $2p \rightarrow 3d$ photon energy region where the effects of both $2p^5(3s^23d + 3s3p^2)$ correlation mixing and spin-orbit mixing of $2p^53s^23d\ {}^1L_J + {}^3L'_J$ states featured, and (2) the photon region just below and straddling over the $2p^{-1}\,{}^2P_{1/2,3/2}$ thresholds where a number of features were attributed to multiply excited configurations with open ionization channels. In the latter region, we also found the $2s \rightarrow 3p$ resonance, almost exclusively in the single-ionization channel. By contrast, the next member, the $2s \rightarrow 4p$ resonance, featured with a strongly asymmetric Fano profile, above the $2p^{-1}\,{}^2P_{1/2,3/2}$ thresholds, in the double-ionization channel only. In general, reasonably good agreement is found between the theoretical results and these observations. However, some notable differences in the strengths of the resonance predictions were observed together with the need for systematic energy shifts. A complete understanding of the finer features just summarized would require separate theoretical studies which are beyond the scope of the present work. Overall, this study on S^{4+} L-shell photoionization, underpins the ongoing need for experimental measurements to benchmark the theoretical models.

ACKNOWLEDGMENTS

The authors thank the SOLEIL beamline staff John Bozek and Aleksandar Milosavljevic for their help during the experiments. T.W.G. was supported in part by NASA (NNX11AF32G).

[1] Chandra x-ray center, https://cxc.harvard.edu/.
[2] XMM-Newton: The x-ray multi-mirror mission a project of the European Space Agency, 2018.
[3] D. Barret, A. Decourchelle, A. Fabian, M. Guainazzi, K. Nandra, R. Smith, and J.-W. den Herder, Astron. Nachr. **341**, 224 (2020).
[4] T. R. Kallman, Space Sci. Rev. **157**, 177 (2010).
[5] T. R. Kallman and P. Palmeri, Rev. Mod. Phys. **79**, 79 (2007).
[6] A. R. Foster, R. K. Smith, N. S. Brickhouse, T. R. Kallman, and M. C. Witthoeft, Space Sci. Rev. **157**, 135 (2010).
[7] D. W. Savin, N. S. Brickhouse, J. J. Cowan, R. P. Drake, S. R. Federman, G. J. Ferland, A. Frank, M. S. Gudipati, W. C. Haxton, E. Herbst, S. Profumo, F. Salama, L. M. Ziurys, and E. G. Zweibel, Rep. Prog. Phys. **75**, 036901 (2012).
[8] S. Nahar, Atoms **8**, 68 (2020).
[9] C. Mendoza, M. A. Bautista, J. Deprince, J. A. García, E. Gatuzz, T. W. Gorczyca, T. R. Kallman, P. Palmeri, P. Quinet, and M. C. Witthoeft, Atoms **9**, 12 (2021).
[10] S. Schippers and A. Müller, Atoms **8**, 45 (2020).
[11] C. Blancard, D. Cubaynes, S. Guilbaud, and J.-M. Bizau, Astrophys. J. **853**, 32 (2018).
[12] S. N. Nahar and A. K. Pradhan, J. Phys. B: At., Mol. Opt. Phys. **26**, 1109 (1993).
[13] D. A. Verner, G. J. Ferland, K. T. Korista, and D. G. Yakovlev, Astrophys. J. **465**, 487 (1996).
[14] P. A. M. van Hoof, G. C. Van de Steene, F. Guzmán, M. Dehghanian, M. Chatzikos, and G. J. Ferland, Contrib. Astron. Obs. Skalnaté Pleso **50**, 32 (2020).
[15] N. R. Badnell, J. Phys.: Conf. Ser. **88**, 012070 (2007).
[16] T. W. Gorczyca, N. R. Badnell, and D. W. Savin, Phys. Rev. A **65**, 062707 (2002).

[17] E. Kennedy, J. Costello, J.-P. Mosnier, and P. van Kampen, Radiat. Phys. Chem. **70**, 291 (2004),.

[18] H. Kjeldsen, J. Phys. B: At., Mol. Opt. Phys. **39**, R325 (2006).

[19] A. Müller, Phys. Scr. **90**, 054004 (2015).

[20] R. B. C. Henry, A. Speck, A. I. Karakas, G. J. Ferland, and M. Maguire, Astrophys. J. **749**, 61 (2012).

[21] N. Kacharov, A. Koch, E. Caffau, and L. Sbordone, Astron. Astrophys. **577**, A18 (2015).

[22] O. L. Dors, E. Pérez-Montero, G. F. Hägele, M. V. Cardaci, and A. C. Krabbe, Mon. Not. R. Astron. Soc. **456**, 4407 (2016).

[23] P. Gorai, *Astrophysics and Space Science Proceedings* (Springer International Publishing, Cham, 2018), pp. 467–475.

[24] S. S. Tayal, Phys. Rev. A **74**, 022704 (2006).

[25] B. Kristensen, T. Andersen, F. Folkmann, H. Kjeldsen, and J. B. West, Phys. Rev. A **65**, 022707 (2002).

[26] V. Stancalie, J. Quant. Spectrosc. Radiat. Transfer **205**, 7 (2018).

[27] K. Butler, C. Mendoza, and C. J. Zeippen, Mon. Not. R. Astron. Soc. **209**, 343 (1984).

[28] J. P. Serrão, J. Quant. Spectrosc. Radiat. Transfer **54**, 447 (1995).

[29] D.-S. Kim and D.-H. Kwon, Phys. Rev. A **88**, 033426 (2013).

[30] T. K. Fang, B. I. Nam, Y. S. Kim, and T. N. Chang, Phys. Rev. A **55**, 433 (1997).

[31] D.-S. Kim and Y. S. Kim, J. Phys. B: At., Mol. Opt. Phys. **41**, 165002 (2008).

[32] J. T. Costello, D. Evans, R. B. Hopkins, E. T. Kennedy, L. Kiernan, M. W. D. Mansfield, J. P. Mosnier, M. H. Sayyad, and B. F. Sonntag, J. Phys. B: At., Mol. Opt. Phys. **25**, 5055 (1992).

[33] M. H. Sayyad, E. T. Kennedy, L. Kiernan, J. P. Mosnier, and J. T. Costello, J. Phys. B: At., Mol. Opt. Phys. **28**, 1715 (1995).

[34] J. B. West, T. Andersen, R. L. Brooks, F. Folkmann, H. Kjeldsen, and H. Knudsen, Phys. Rev. A **63**, 052719 (2001).

[35] C. E. Hudson, J. B. West, K. L. Bell, A. Aguilar, R. A. Phaneuf, F. Folkmann, H. Kjeldsen, J. Bozek, A. S. Schlachter, and C. Cisneros, J. Phys. B: At., Mol. Opt. Phys. **38**, 2911 (2005).

[36] L. Hernández, A. Covington, E. Hernández, A. Antillón, A. Morales-Mori, K. Chartkunch, A. Aguilar, and G. Hinojosa, J. Quant. Spectrosc. Radiat. Transfer **159**, 80 (2015).

[37] J.-P. Mosnier, M. H. Sayyad, E. T. Kennedy, J.-M. Bizau, D. Cubaynes, F. J. Wuilleumier, J.-P. Champeaux, C. Blancard, R. H. Varma, T. Banerjee, P. C. Deshmukh, and S. T. Manson, Phys. Rev. A **68**, 052712 (2003).

[38] J. Bizau, D. Cubaynes, S. Guilbaud, N. E. Eassan, M. A. Shorman, E. Bouisset, J. Guigand, O. Moustier, A. Marié, E. Nadal, E. Robert, C. Nicolas, and C. Miron, J. Electron Spectrosc. Relat. Phenom. **210**, 5 (2016).

[39] L.-M. Ren, Y.-Y. Wang, D.-D. Li, Z.-S. Yuan, and L.-F. Zhu, Chin. Phys. Lett. **28**, 053401 (2011).

[40] H. Friedrich, *Theoretical Atomic Physics* (Springer-Verlag, Berlin Heidelberg, 2006).

[41] J. Bruneau, J. Phys. B **17**, 3009 (1984).

[42] I. P. Grant, J. Phys. B **7**, 1458 (1974).

[43] J. Slater, *Quantum Theory of Molecules and Solids Vol. 4: The Self-Consistent Field for Molecules and Solids* (McGraw Hill, New York, 1974).

[44] T. W. Gorczyca, M. A. Bautista, M. F. Hasoglu, J. García, E. Gatuzz, J. S. Kaastra, T. R. Kallman, S. T. Manson, C. Mendoza, A. J. J. Raassen, C. P. de Vries, and O. Zatsarinny, Astrophys. J. **779**, 78 (2013).

[45] A. E. Kramida, Y. Ralchenko, J. Reader, and NIST Atomic Spectra Database, National Institute of Standards and Technology (2020), http://physics.nist.gov/asd.

[46] P. G. Burke, *R-Matrix Theory of Atomic Collisions* (Springer, New York, 2011).

[47] K. A. Berrington, W. B. Eissner, and P. H. Norrington, Comput. Phys. Commun. **92**, 290 (1995).

[48] T. W. Gorczyca and F. Robicheaux, Phys. Rev. A **60**, 1216 (1999).

[49] J.-P. Mosnier, E. T. Kennedy, J.-M. Bizau, D. Cubaynes, S. Guilbaud, C. Blancard, and B. M. McLaughlin, Atoms **9**, 27 (2021).

[50] E. Condon and G. Shortley, *The Theory of Atomic Spectra* (Cambridge University Press, Cambridge, UK, 1987 Reprint), Chap. XV, pp. 366–367.

[51] N. Badnell, Comput. Phys. Commun. **182**, 1528 (2011).